JACS
JOURNAL OF THE AMERICAN CHEMICAL SOCIETY
Article
pubs.acs.org/JACS

Transformation of Sintered $CsPbBr_3$ Nanocrystals to Cubic $CsPbI_3$ and Gradient $CsPbBr_xI_{3-x}$ through Halide Exchange

Jacob B. Hoffman,[‡,†] A. Lennart Schleper,[‡,†,⊥] and Prashant V. Kamat*[,‡,†,§]

[‡]Radiation Laboratory, [†]Department of Chemistry and Biochemistry, and [§]Department of Chemical and Biomolecular Engineering, University of Notre Dame, Notre Dame, Indiana 46556, United States

Supporting Information

ABSTRACT: All-inorganic cesium lead halide ($CsPbX_3$, X = Br^-, I^-) perovskites could potentially provide comparable photovoltaic performance with enhanced stability compared to organic–inorganic lead halide species. However, small-bandgap cubic $CsPbI_3$ has been difficult to study due to challenges forming $CsPbI_3$ in the cubic phase. Here, a low-temperature procedure to form cubic $CsPbI_3$ has been developed through a halide exchange reaction using films of sintered $CsPbBr_3$ nanocrystals. The reaction was found to be strongly dependent upon temperature, featuring an Arrhenius relationship. Additionally, film thickness played a significant role in determining internal film structure at intermediate reaction times. Thin films (50 nm) showed only a small distribution of $CsPbBr_xI_{3-x}$ species, while thicker films (350 nm) exhibited much broader distributions. Furthermore, internal film structure was ordered, featuring a compositional gradient within film. Transient absorption spectroscopy showed the influence of halide exchange on the excited state of the material. In thicker films, charge carriers were rapidly transferred to iodide-rich regions near the film surface within the first several picoseconds after excitation. This ultrafast vectorial charge-transfer process illustrates the potential of utilizing compositional gradients to direct charge flow in perovskite-based photovoltaics.

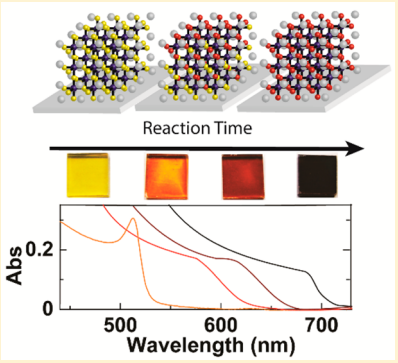

INTRODUCTION

Organic–inorganic methylammonium lead halide ($MAPbX_3$, X = Br^-, I^-) perovskite structure semiconductors have emerged as attractive options for light harvesting materials.[1−5] Specifically, $MAPbI_3$ has shown the most promise for high-efficiency solar cells, reaching power conversion efficiencies (PCEs) over 22% in 2016.[6] While clearly possessing many properties favorable for light harvesting,[7−16] concerns have been raised about the stability of $MAPbI_3$ under exposure to humidity, oxygen, and heat.[17−22]

One proposal to improve device stability is to replace the organic component with inorganic cesium, forming fully inorganic cesium lead halide perovskite ($CsPbX_3$, X = Br^-, I^-).[23−27] In particular, Hodes et al. have been able to achieve significantly increased device stability while maintaining comparable PCE versus $MAPbBr_3$.[28,29] While these results suggest that high PCE devices can be made using Cs^+ as a cation, current deposition methods for $CsPbBr_3$ are limited by the poor solubility of CsBr.[29,30] Additionally, the relatively large bandgap (2.36 eV) of $CsPbBr_3$ limits the theoretical PCE of $CsPbBr_3$-based photovoltaic devices.[29,31] The cubic phase of $CsPbI_3$ has a reported band gap of 1.73 eV,[32] absorbing most of the visible region of the solar spectrum. However, this structure only forms at high temperatures (~310 °C) and typically degrades into the wide bandgap (3.01 eV) orthorhombic non-perovskite phase shortly after fabrication.[33−36] This has led to major problems with device fabrication as the orthorhombic phase tends to form during film annealing and when exposed to ambient conditions.[23,35] To date, only Snaith and co-workers have been able to produce a cubic $CsPbI_3$ solar cell, but have failed to achieve PCEs over 3%.[35] One way to circumvent phase stability issues associated with direct deposition is through halide exchange. Halide exchange has been demonstrated in bulk $MAPbX_3$,[37−39] as well as suspended $CsPbX_3$ nanocrystals,[40,41] but has not been shown for bulk $CsPbX_3$ species.

In this report, we develop an alternative layer-by-layer deposition procedure for bulk $CsPbBr_3$ through sintering of $CsPbBr_3$ nanocrystals (NCs).[42] We demonstrate these bulk $CsPbBr_3$ films readily undergo halide exchange when submerged in a heated lead iodide solution to form bulk cubic $CsPbI_3$. Furthermore, we show that partially exchanged films feature a $CsPbBr_xI_{3-x}$ compositional gradient that is customizable by adjusting film thickness and exchange time. From transient absorption measurements of the compositional gradient we elucidate ultrafast charge carrier migration to iodide-rich regions and discuss the implications of such an internal structure in $CsPbBr_xI_{3-x}$ photovoltaics.

EXPERIMENTAL SECTION

Materials. Acetone (HPLC grade, Fischer Scientific), ethanol (200 proof, anhydrous, Koptec), *n*-heptane (99%, spectrophotometric grade, Sigma-Aldrich), *n*-hexane (95%, anhydrous, Sigma-Aldrich), cesium carbonate (Cs_2CO_3, 99.9%, metals basis, Alfa Aesar), lead(II) bromide ($PbBr_2$, 98%, Sigma-Aldrich), lead(II) iodide (PbI_2, 99.999%,

Received: May 5, 2016
Published: June 20, 2016

DOI: 10.1021/jacs.6b04661
J. Am. Chem. Soc. 2016, 138, 8603−8611

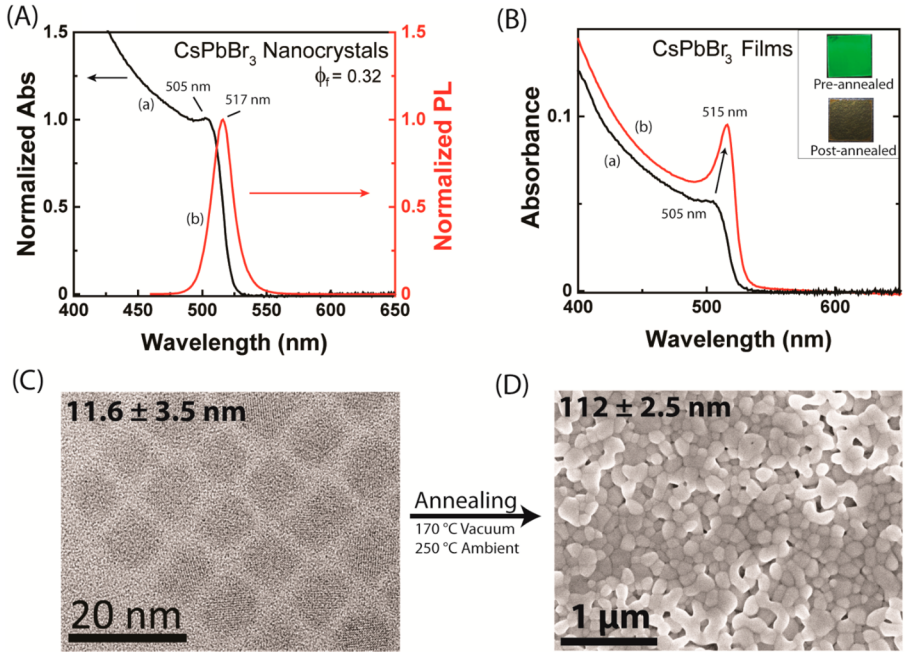

Figure 1. (A) Normalized (a) absorption (505 nm) and (b) photoluminescence (PL) (517 nm) spectra (440 nm excitation) of $CsPbBr_3$ NCs featuring a PL quantum yield of 0.32 (vs Rhodamine 6G). (B) Absorption of $CsPbBr_3$ films (a) pre- and (b) post-annealing. The shift in absorption is consistent with the formation of bulk $CsPbBr_3$. Inset: Pictures of pre- (top) and post-annealed (bottom) $CsPbBr_3$ films against a black background under UV-excitation illustrating PL quenching upon annealing. (C) TEM (20 nm scale) of $CsPbBr_3$ NCs and (D) top-down SEM (1 μm) of a post-annealed $CsPbBr_3$ film. The average crystal diameter grew from 11.6 ± 3.5 nm to 112 ± 2.5 nm indicating that the annealing process sintered the nanoparticles into bulk crystallites.

trace metals basis, Sigma-Aldrich), 1-octadecene (ODE) (95%, Sigma-Aldrich), oleic acid (OAc) (technical grade, 90%, Sigma-Aldrich), oleylamine (OAm) (technical grade, 70%, Sigma-Aldrich), and titanium dioxide paste (Ti-Nanoxide T/SP, solaronix) were used without further purification. VWR Microscope Slides (1 mm thickness) were sonicated in ethanol for 5 min followed by oxygen plasma cleaning for 5 min.

Synthesis and Purification of $CsPbBr_3$ Nanocrystals. Synthesis of $CsPbBr_3$ NCs followed a route recently published by Kovalenko et al. with minor alterations.[42] A precursor solution of cesium oleate (Cs-oleate) was prepared in a 25 mL 3-neck flask where Cs_2CO_3 (0.61 g) was suspended in OAc (1.5 mL) and ODE (10 mL). The suspension was heated up to 100 °C and degassed for 1 h. After degassing the suspension was put under nitrogen atmosphere and heated up to 135 °C until Cs_2CO_3 was fully dissolved. The Cs-oleate was then kept at 150 °C to ensure it remained dissolved. In another 25 mL 3-neck flask $PbBr_2$ (0.21 g) was suspended in OAc (3 mL) and purged at 100 °C for 1 h. The reaction mixture was put under nitrogen atmosphere and heated up to 210 °C where OAm (3 mL) was added. After $PbBr_2$ was fully dissolved and the solution had recovered to 210 °C, 1 mL of 150 °C Cs-oleate precursor was injected. After 10 s the reaction was cooled down to 60 °C by using an ice water bath, and 10 mL of ODE was injected to prevent OAc and OAm from freezing.

The precipitated NCs were separated from the reaction mixture via centrifugation at 7800 rpm for 10 min. Excess ligand was removed by rinsing the resulting pellet with 5 mL ODE followed by centrifugation. The supernatant was again discarded and the pellet was rinsed with acetone to remove excess ODE. The NCs were then re-suspended in 90% hexane/10% heptane and re-centrifuged to remove any non-suspended material.

Preparation of $CsPbBr_3$ Films. Mesoporous TiO_2 was applied via spin-casting a TiO_2−ethanol dispersion (2:7 wt%) at 5000 rpm for 30 s onto a 2.5 × 2.5 cm clean glass substrate followed by thermal treatment at 500 °C for 60 min. Each layer of $CsPbBr_3$ was applied by dynamically spin-casting 30 μL of NC solution for 20 s at 5000 rpm. The sample was then thermally treated in a vacuum oven at 170 °C for 5 min and then on a hot plate at 250 °C under ambient conditions for another 5 min. After cooling down to room temperature the next layer of $CsPbBr_3$ was applied until the desired film thickness was reached. Film thickness was found using a Bruker DektakXT profilometer. Samples prepared for XRD, and transient absorption spectroscopy were covered with a layer of poly(methyl methacrylate) (PMMA) to prevent sample degradation from exposure to humidity. This protective layer was applied through spin coating a solution of PMMA in chlorobenzene (10 mg/mL) at 2000 rpm for 30 s in a nitrogen-filled glovebox.

Halide Exchange Reaction. Halide exchange was performed by soaking $CsPbBr_3$ films in a PbI_2 solution (14 mM, iodide) heated via oil bath or Peltier (*in situ* experiments only). The solution was made by heating PbI_2 (68 mg), OAm (0.6 mL), OAc (0.4 mL), and ODE (20 mL) at 170 °C until PbI_2 dissolved.

Optical Measurements. *In Situ Absorption.* A Cary 50 bio spectrophotometer was used to monitor the halide exchange in real time. A 2.0 × 0.8 cm $CsPbBr_3$ film was placed in a quartz cuvette filled with 1.5 mL of PbI_2 solution. The solution temperature was controlled via a Peltier located within the cuvette holder. Thin, 50 nm films were used to ensure minor contributions from varied internal film structure and to stay within the linear region of the Beer−Lambert law. The instrument was baselined with a TiO_2 substrate in the soaking solution at the exchange temperature prior to data collection.

Transient Absorption Spectroscopy. Transient absorption spectroscopy was performed using a Clark MXR-2010 laser system (775 nm fundamental, 1 mJ/pulse, fwhm =150 fs, 1 kHz repetition rate) with Helios software from Ultrafast Systems on thick 350 and thin 25 nm halide exchanged films. The fundamental was separated 95/5. The 95% portion became the pump, and was frequency doubled to generate 387 nm excitation. The pump power density for all experiments was kept below 4 $\mu J/cm^2$ to minimize carrier interactions using a variable neutral density filter and an iris of known diameter. These conditions also inhibited photoinduced phase separation. The 5% portion was sent through a CaF_2 crystal to generate a white light continuum, after which excess fundamental was removed using a short-pass filter.

DOI: 10.1021/jacs.6b04661
J. Am. Chem. Soc. 2016, 138, 8603−8611

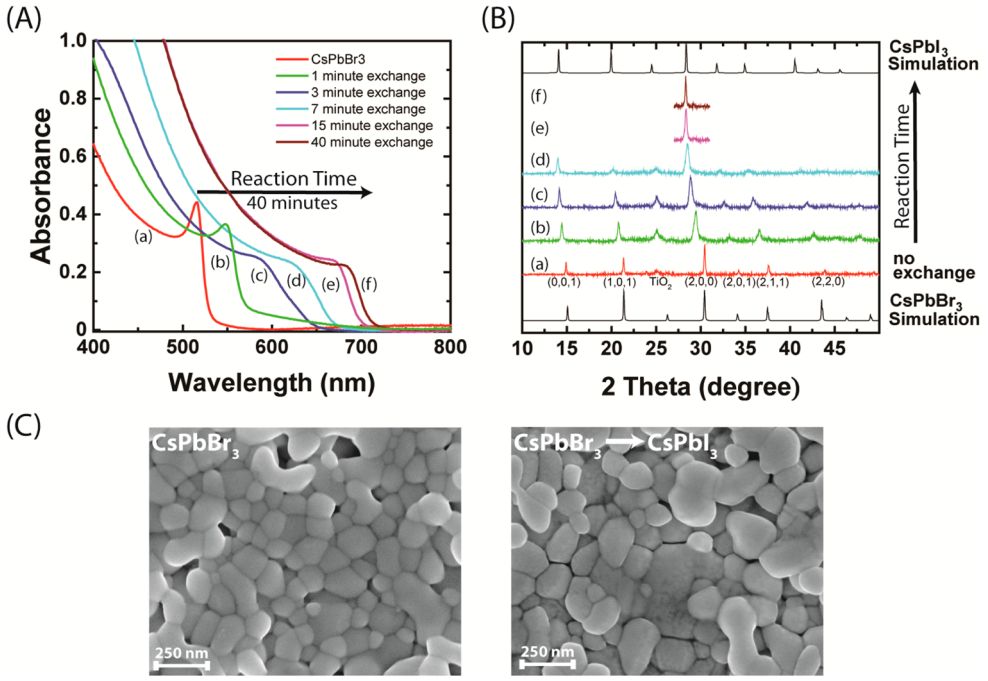

Figure 2. (A) Absorption spectra of annealed films at different points in the halide exchange reaction: (a) 0, (b) 1, (c) 3, (d) 7, (e) 15, and (f) 40 min. (B) XRD of the same films showing a shift in diffraction peaks consistent with $CsPbBr_3$ and $CsPbI_3$ simulations.[53] No additional peaks appearing in the spectra indicate that $CsPbI_3$ remains in the cubic phase. (C) Top-down SEM images of $CsPbBr_3$ and post-exchanged $CsPbI_3$ films. There is no major change in film morphology from the exchange, including no new crystals forming on the surface.

Photoluminescence Measurements. Photoluminescence quantum yield of $CsPbBr_3$ NCs was found using a Rhodamine 6G standard in ethanol (φ_f = 95%) at 457 nm excitation in a Jobin Yvon Fluorolog-3 (1 nm slits). Spectra were corrected for the inner filter effect.[43]

Powder X-ray Diffraction (XRD). Powder XRD experiments were done using a Bruker D8 Discover diffractometer in Bragg–Brentano geometry with a Cu X-ray source (λ = 1.5418 Å) on 75 nm thick exchanged films. Samples were prepared through anion exchange at 120 °C for different amounts of soaking time (1 min, 3 min, 7 min, 15 min, 40 min). Measurements were taken over the range of 10–50° with a step size of 0.02° and an integration time of 2 s. For the 15 and 40 min samples, a smaller range was used (27–31°) due to sample degradation during data collection.

Electron Microscopy. Transmission electron microscopy (TEM) images of $CsPbBr_3$ NCs were obtained with a FEI Titan 80–300 microscope operated at 300 keV. The compositional depth profile was accomplished by altering a previously described method.[44] In short, a 100 nm thick cross section was cut from the 40 min exchanged film using a focused ion beam. The obtained cross section was imaged in STEM mode, and then the electron beam (beam size ~1 nm) was rastered collecting EDX data (Oxford Inca EDX detector) as a function of film depth. Scanning electron microscopy (SEM) images (top-down and cross-sectional) were captured using a FEI-Magellan 400 scanning electron microscope with a Schottky field emitter source mounted on the gun module.

RESULTS AND DISCUSSION

Fabrication of $CsPbBr_3$ Films from Suspended Nanocrystals. $CsPbX_3$ NCs have recently emerged as an exciting material for lighting and lasing applications due to excellent photoluminescence (PL) quantum yield, bandgap tunability, and photostability when deposited onto substrates via both spin or drop casting.[42,45,46] Fusing NCs through thermal treatment has been utilized as a way to obtain bulk films for cadmium and lead chalcogenide quantum dots.[44,47,48] Similarly, we expected $CsPbBr_3$ NCs to readily sinter, due to weak binding between $CsPbBr_3$ NCs and passivating ligand species,[49] coupled with reported self-assembly of $CsPbBr_3$ nanostuctures.[50]

To examine the aspects of film formation, we synthesized $CsPbBr_3$ NCs following a modified hot injection procedure from Kovalenko and co-workers.[42] Immediately after synthesis, NCs were cleaned of excess ligand (see Experimental Section) and suspended in a 90% hexane 10% heptane solution. Synthesized NCs exhibit an absorption peak at 505 nm along with strong PL (φ_f = 0.32) centered at 516 nm (Figure 1A). Despite a narrow fwhm (19 nm), TEM imaging revealed the NCs feature a relatively broad size distribution with an average cube length of 11.6 ± 3.5 nm (Figure 1C) (FigureS1 for additional TEM images and size distribution). The removal of excess ligands and suspension of NCs in the hexane/heptane mixed solvent allow NCs to be readily spin-cast onto mesoporous TiO_2 films. It is interesting to note that NCs agglomerate as crystallites on the surface of TIO_2 rather than permeate into the mesoporous structure as evidenced by cross-sectional SEM (Figure S2). Spin-cast NC films retain the initial absorption and PL peaks of NCs in solution (Figure 1B(a)). To obtain bulk $CsPbBr_3$, NCs deposited on mesoporous TiO_2 were annealed at 170 °C (5 min) under vacuum followed by additional annealing at 250 °C (5 min) under ambient conditions. These annealed films were insoluble in the hexanes/heptane NC solution, thus allowing for the deposition of additional NC cycles until the desired film thickness was reached (Figure S3).

Comparison of the steady-state absorbance properties of pre-annealed and post-annealed films shows a 10 nm red-shift in the absorption peak (Figure 1B). A similar red-shift is observed in the PL spectrum (Figure S4), but PL intensity is almost entirely quenched by the annealing process (Figure 1B inset). The changes in absorption and PL peaks are consistent with a transformation from quantum confined NCs to bulk material.

DOI: 10.1021/jacs.6b04661
J. Am. Chem. Soc. 2016, 138, 8603–8611

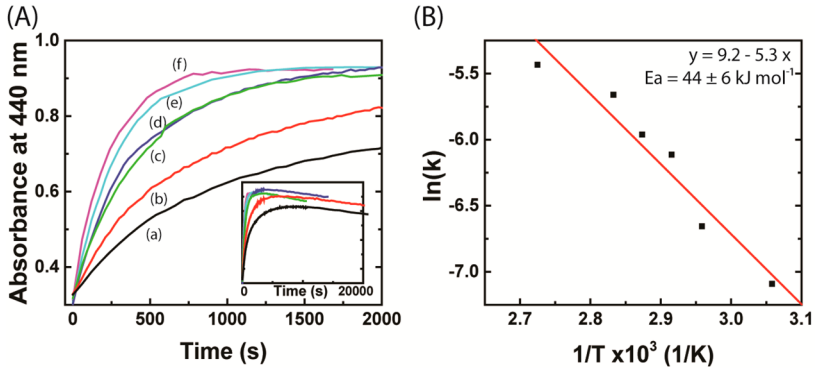

Figure 3. (A) Halide exchange reaction kinetics from *in situ* UV−visible experiments at different temperatures: (a) 56, (b) 64, (c) 70, (d) 75, (e) 79, and (f) 94 °C. Kinetics were fit to a mono-exponential equation, typical of a pseudo-first-order reaction. Inset: On longer time scales film absorbance decreased due to excess ligand coordinating to Cs^+ and Pb^{2+} cations. (B) The obtained rate constants follow an Arrhenius relationship, yielding an activation energy of 44 ± 6 kJ/mol.

The post annealed Tauc gap features a direct bandgap of 2.36 eV (Figure S5), matching with the reported value from Hodes and co-workers.[29] Figure 1D shows a top-down SEM image of an annealed spin coated film with average crystallite diameter of 112 ± 2.5 nm calculated via the intercept method (Figure S6). The increase in crystallite size shows that NCs grow to well outside the dimensions of quantum confinement upon sintering.[42] It is interesting to note that along with the absorption and PL red-shift a sharp peak at the band edge appeared upon annealing, indicating a stronger excitonic transition. The stronger excitonic peak is similar to the more prominent excitonic peak observed by Petrozza and co-workers for $MAPbI_3$ when deposited as a planar film versus when confined in mesoporous Al_2O_3.[51,52] In that study, the increased excitonic contribution of planar films was attributed to decreased crystal surface area, which could explain the absorption changes observed when high surface area NCs sinter into bulk.

Transformation of Cubic $CsPbBr_3$ to Cubic $CsPbI_3$ through Halide Exchange. $CsPbX_3$ NCs have been shown to form in the cubic crystal phase, including $CsPbI_3$ which is expected to form in the orthorhombic phase at the synthesis temperatures reported.[36] This behavior has been previously attributed to lower NC surface energies stabilizing the cubic product.[42] Post annealed $CsPbBr_3$ films fabricated here retain the initial crystal structure of the NCs, as confirmed by X-ray diffraction (XRD) peaks matching cubic $CsPbBr_3$ without noticeable contamination from synthesis precursors (Figure 2B(a)). Based on these observations we anticipated that films of bulk $CsPbI_3$ could be fabricated from NCs using the same approach in the previous section. However, films of spin-casted $CsPbI_3$ NCs formed into the orthorhombic phase upon annealing (Figure S7). We attribute the phase change to be triggered by an increase in surface energy during sintering of $CsPbI_3$ NCs.

We adopted an alternative method to obtain cubic $CsPbI_3$ by employing a bromide to iodide halide exchange reaction. Annealed $CsPbBr_3$ films of approximately 75 nm thickness were soaked in a PbI_2 solution dissolved in 1-octadecene, oleylamine, and oleic acid, at a solution temperature of 75 °C (see experimental section for additional details). With increased exposure to the PbI_2 solution we observe film absorbance continually red-shifting (Figure 2A) until reaching an optical band gap of 1.76 eV (Figure S5), close to the value reported for cubic $CsPbI_3$.[54] Although the absorption red-shift indicates formation of cubic $CsPbI_3$, additional analysis was needed to confirm that the cubic phase is the sole product of the exchange reaction. Powder XRD shows diffraction peaks shift to smaller degrees with increased exchange times (Figure 2B). The total shift of the (2,0,0) diffraction peak is 2.2 degrees, signifying an increase of lattice volume from 199.2 to 236.0 $Å^3$ (Figure S8A). This is consistent with the lattice parameters previously reported for cubic $CsPbI_3$, signifying a full exchanged occurred.[53] No additional diffraction peaks appear in the spectra, confirming that the $CsPbI_3$ crystal structure remains cubic throughout the exchange.

Following exchange, all films remained in the cubic phase when stored in dry environments with no observable degradation. However, similar to what was reported by Snaith et al., films with significant iodide content begin to degrade into the orthorhombic phase under ambient conditions.[35] This is reflected in orthorhombic $CsPbI_3$ diffraction peaks appearing upon multiple sequential XRD scans (Figure S8B). We speculate that this phase change is closely tied to humidity exposure as all films were indefinitely stable in dry environments. The morphology of the film did not significantly change before and after the exchange reaction (Figure 2C). This is in stark contrast to what was observed by Grätzel et al. for $MAPbBr_3$ to $MAPbI_3$ halide exchange employing a soaking solution, where distinct crystals of $MAPbI_3$ formed on top of the pre-existing $MAPbBr_3$.[38] The lack of crystal growth on the film surface shows that all changes in film properties come from halide exchange, and not formation of new product on the film surface.

Temperature Dependence of the Halide Exchange Reaction. In $CsPbBr_3$ films, halide exchange did not visibly progress at room temperature, contrary to the ambient conditions used for previously reported $MAPbX_3$ exchanges.[38,39] The rate of halide exchange in the present experiments was investigated using *in situ* UV−visible absorbance measurements at constant soaking solution temperatures ranging from 55 to 94 °C. Reaction progress was monitored through change in absorbance at 440 nm, with an initial value of 0.3 (pure $CsPbBr_3$) and final value of 0.9 (pure $CsPbI_3$) for 50 nm thick films (Figure 3A).

The halide exchange reaction showed a significant dependence on the temperature of the PbI_2 soaking solution. The reaction featured mono-exponential kinetics at high exchange temperatures (79 and 94 °C). This is characteristic of a pseudo-first order reaction with iodide in excess, and consistent with

DOI: 10.1021/jacs.6b04661
J. Am. Chem. Soc. 2016, 138, 8603−8611

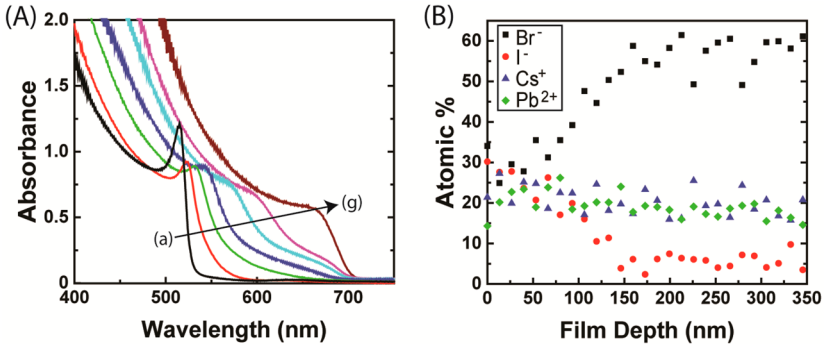

Figure 4. (A) UV−visible absorption spectra of 350 nm thick $CsPbBr_3$ films soaked in 120 °C PbI_2 solution for (a) 0, (b) 5, (c) 15, (d) 30, (e) 60, (f) 150, and (g) 480 min. Film thickness impacted the reaction by making diffusional processes more relevant. (B) EDX depth profile of the 30 min exchanged film showing that iodide present in the film quickly drops to instrument noise levels by 150 nm, clearly indicating a composition gradient present in the film.

the observed kinetics for solution-based halide exchange with $MAPbX_3$.[38] At lower temperatures, the increase in absorbance from halide exchange was convoluted with a slow overall loss of absorbance (Figure 3A inset). This was attributed to film etching from excess ligand coordinating to Pb^{2+} and Cs^+ cations (Figure S9). The remaining pseudo-first-order reaction rate constants were determined by extrapolating a mono-exponential fit using the first 500 s of the exchange (Figure S10), before film dissolution made a significant impact on the absorption growth.

The stark dependence of rate on temperature indicates a significant activation energy barrier for the halide exchange. We found the activation energy for the exchange using the Arrhenius eq (eq 1),

$$\ln(k) = \ln(A) - \frac{E_A}{RT} \quad (1)$$

where k is the reaction rate constant, A is a pre-exponential factor, E_A is the activation energy, R is the universal gas constant, and T is the absolute solution temperature. The natural log of the obtained pseudo-first order rate constants plotted against the inverse of solution temperature followed the linear trend expected from eq 1 (Figure 3B). The resulting slope from the linear fit yielded an activation energy of 44 ± 6 kJ mol^{-1} (0.46 ± 0.06 eV). This apparent activation energy represents the energy required to expand the lattice to incorporate iodide anions. The reverse reaction (iodide to bromide) progressed significantly faster at the same temperature (Figure S11), suggesting less energy is required to replace iodide with smaller bromide.

Variation in Internal Film Composition in Thicker Films. In the previous sections, we showed band edge absorbance in thin films continually red-shifts during the exchange reaction as opposed to independent $CsPbI_3$ absorbance growing in at low energy regions. This observation was suggestive of a gradual stepwise exchange for the 75 nm films used with film composition remaining homogeneous. However, an absorption tail (Figure 2A(b−d)) coupled with broadened X-ray diffraction peaks (Figure S8A) at intermediate reaction times indicated a small distribution of $CsPbBr_xI_{3-x}$ present. Bulk ion exchange has been shown to strongly depend on diffusion of the exchanging species within the film.[55,56] Thus, we expect film thickness to play an integral role in determining internal film structure.

To better understand how halide exchange impacts internal film structure we studied halide exchange in thicker films (350 nm). UV−visible absorption spectra for the thicker films shown in Figure 4A has significantly different features than thinner films. After 15 min of film soaking (spectrum c), the main absorbance peak red-shifts only ~20 nm, but an absorbance tail stretching across the entire $CsPbBr_xI_{3-x}$ range is also present. This tail in the absorption spectra indicates a much broader distribution of $CsPbBr_xI_{3-x}$ present than the thin film case.

The broadened absorbance suggests a heterogeneous film, but does not give insight into internal film structure. Thus, elemental composition as a function of depth was obtained from a cross section (Figure S12) of the 30 min exchanged film (Figure 4B). As expected, the atomic percent of lead and cesium were approximately 20% throughout the film. However, the relative concentrations of iodide and bromide varied drastically. The ratio of iodide:bromide at the film surface was approximately one. However, the percentage of iodide gradually decreased to within instrument noise by 150 nm, showing that the film was mostly unreacted. This gradual tapering of iodide clearly indicates the presence of a distinct compositional gradient at intermediate reaction times.

The increased variation in internal film structure with increased film thickness arose from the role of anion diffusion in the exchange reaction. The exchange reaction progresses in three steps: diffusion of iodide to the film/solution interface, anion exchange at the film solution interface, and internal iodide diffusion (Scheme 1A). Similar to $MAPbI_3$ to $MAPbBr_3$ exchange,[38] iodide diffusion to the film surface is not rate limiting, as varying iodide concentration in solution does not significantly impact the exchange reaction rate (Figure S13). Thus, the exchange reaction in our experimental setup is likely governed by the remaining two steps. After exchange with bromide, newly incorporated iodide must diffuse away from the film/solution interface, or iodide concentration will build up at the crystal surface. In the 75 nm films, iodide was able to diffuse throughout the entire film effectively, leading to only minor variation in film composition (Scheme 1B). When film thickness increased to 350 nm, iodide could not diffuse through the entire film as quickly as new iodide entered the film at the interface, leading to the observed compositional gradient developing.

Transient Absorption of Exchanged Films. Halide exchange of $CsPbBr_3$ films provides routes to design hybrid $CsPbBr_xI_{3-x}$ with the resulting internal structures determined by initial film thickness and duration of the exchange. How this

DOI: 10.1021/jacs.6b04661
J. Am. Chem. Soc. 2016, 138, 8603−8611

Scheme 1. (A) Three-Step Halide Exchange Reaction: Iodide Diffusion to the Film/Solution Interface, Exchange with Bromide and the Interface, and Internal Iodide Diffusion Away from the Interface; (B) Differences in Internal Film Structure between Thin (75 nm) and Thick (350 nm) Exchanged Films[a]

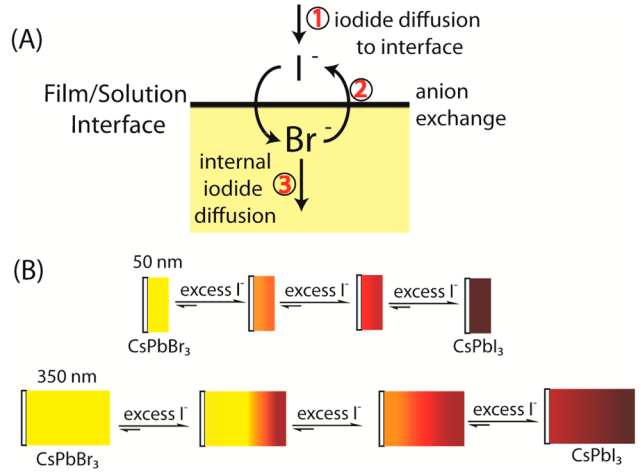

[a]As film thickness increases iodide has further to diffuse within the film allowing an internal compositional gradient to develop.

variation in film structure impacts the excited state can be probed with transient absorption spectroscopy. $CsPbBr_3$ films with a thickness of either 25 or 350 nm exchanged with iodide ions allowed us to investigate cases with and without a significant compositional gradient present. Power density of the pump laser pulse (387 nm) was kept low (<4 $\mu J/cm^2$) to inhibit photoinduced phase separation that has been shown to occur in both $MAPbBr_xI_{3-x}$ and $CsPbBr_xI_{3-x}$ species.[23,57]

Figure 5A shows the difference absorption spectra of 25 nm thick films at various stages of halide exchange at a 10 ps pump/probe delay (for full time-resolved spectra see Figure S14). The difference absorption spectrum of $CsPbBr_3$ (a) displays a strong bleach at 517 nm corresponding to the band edge of $CsPbBr_3$. As the film became rich with iodide (spectra b–f), the main bleach red-shifts, agreeing with the observed trend in steady-state absorbance. It is interesting to note how close the difference absorption spectra of $CsPbX_3$ mirrors corresponding $MAPbX_3$ spectra featuring a strong band edge bleach paired with a weaker bleach at higher energies (only visible for spectra c–f).[58] These similarities illustrate that MA^+ and Cs^+ electronic levels have little contribution to the evolving excited state. This observation matches the expected electronic structure where conduction and valence bands are dominated by lead and halide contributions respectively, leading to an excited state dominated by lead and halide.[53,59] At the initial stages of halide exchange, kinetics of charge recombination as monitored at the bleach maximum become drastically faster (Figure 5B(a,b)). With increased exchange time, the bleach exhibited slower recombination (c–f). This trend was corroborated by film PL (Figure S15), signifying large amounts of non-radiative recombination introduced with small amounts of iodide.

In thicker films (350 nm) transient spectra were distinctly different as compared to thin films, arising from the inhomogeneous distribution of anions. The spectral differences are best illustrated using the 15 min soaked 350 nm film in transient absorption measurements under two excitation configurations: forward and reverse side (Figure 6) (spectra of additional soaking times in Figure S16). When excited from the reverse side (Figure 6A) the transient spectra exhibits a narrow bleach at 535 nm matching the observed steady-state absorption peak. The transient spectra captured at different delay times does not exhibit any change in the peak position suggesting the involvement of a single excited species. When the excitation was switched toward the forward side (Figure 6B), the transient absorption spectrum recorded at a delay of 0.5 ps features a broad main bleach across the visible region (545–610 nm), which shifts to low-energy regions with increased delay times.

Distinct differences in the transient absorption spectra recorded with excitation from opposite sides arise from the high absorbance of the films at 387 nm leading to inhomogeneous absorption of the pump at different film depths (Figure 6C). Pump penetration depth was estimated from the measured absorbance coefficient of pure $CsPbBr_3$ at 387 nm (150 000 ± 17 000 cm^{-1}) to be approximately 67 nm (Figure S17). This estimation is clearly the upper limit of penetration depth, due to the higher absorbance of the partially exchanged portion of the film. However, it illustrates what film regions are excited from the reverse versus the forward directions. From the reverse side, the majority of the pump excites the film region that is minimally impacted by halide

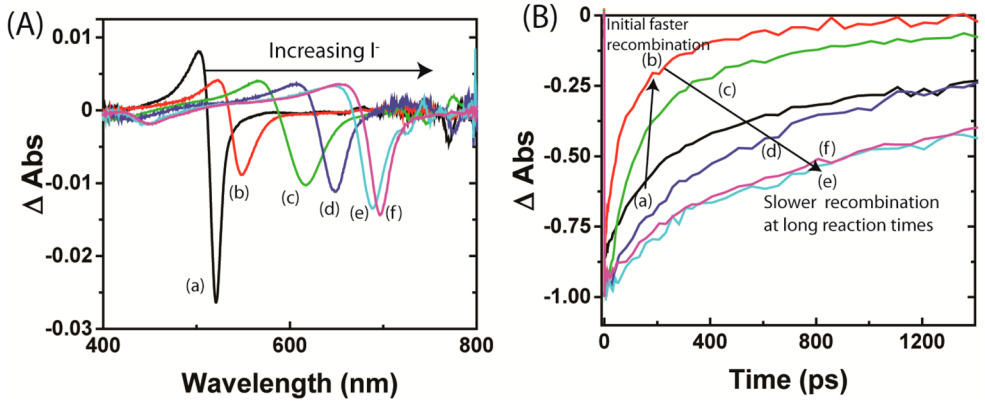

Figure 5. (A) Difference absorption spectra at 10 ps delay for 25 nm thick films soaked at 120 °C for (a) 0 s, (b) 10 s, (c) 30 s, (d) 1 min, (e) 3 min, (f) 25 min. (B) Kinetic traces recorded at the main bleach maxima for the same films. At short exchange times the bleach kinetics become significantly faster, but slowed as more iodide was introduced.

DOI: 10.1021/jacs.6b04661
J. Am. Chem. Soc. 2016, 138, 8603–8611

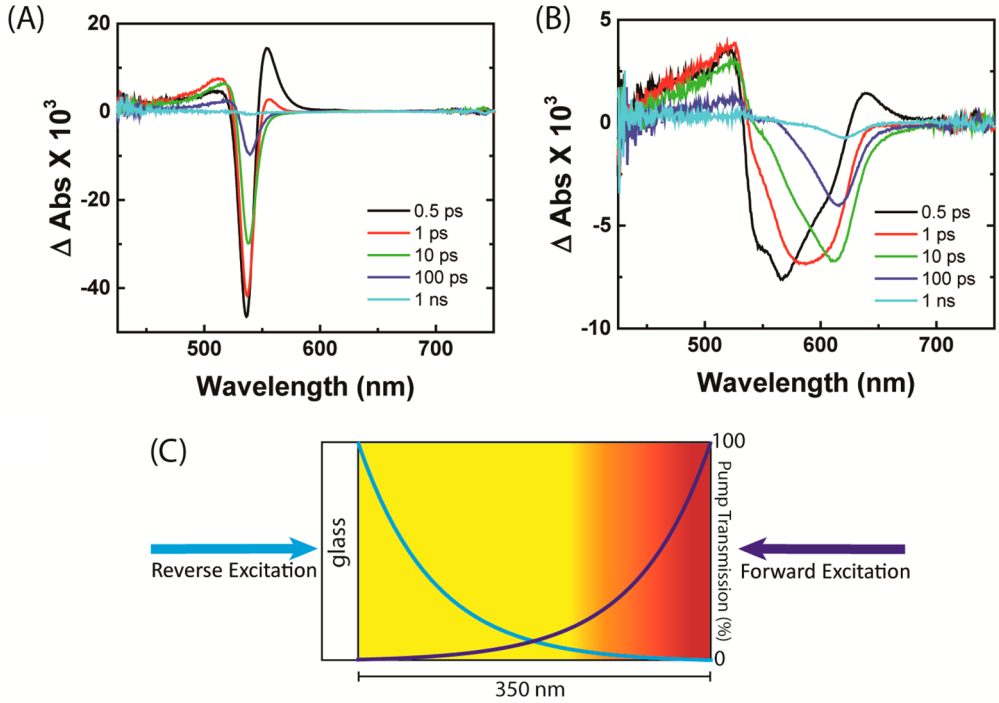

Figure 6. Difference absorption spectra of (A) reverse and (B) forward excitation of the 15 min soaked 350 nm thick film. Reverse excitation matches what is expected from the steady-state absorption peak (Figure 4A(d)), indicating that the feature originates deep within the minimally exchanged portion of the film. Forward excitation shows the bleach moving across the visible spectrum, suggesting focused excitation on the film surface near the compositional gradient. (C) Schematic showing experimental setup of thick film transient absorption experiments. The 387 nm pump is completely absorbed by the film with a maximum estimation of penetration depth of 67 nm. This leads to the significant differences in where the pump is absorbed within the film when exciting from the forward or reverse direction.

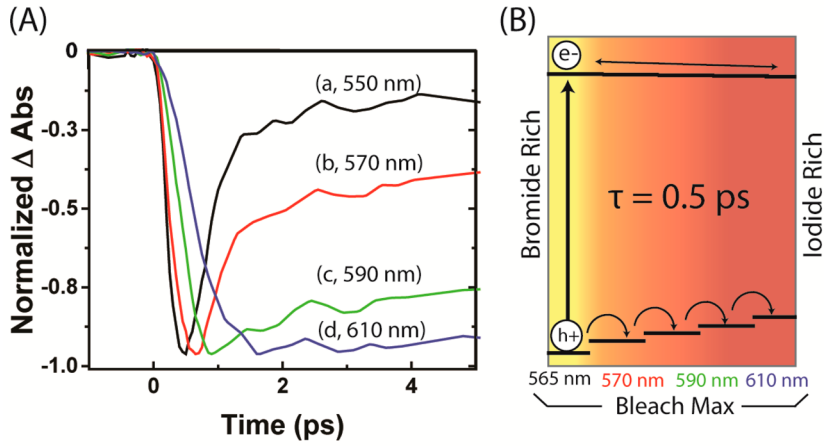

Figure 7. (A) Transient absorption kinetics of Figure 6B at (a) 550, (b) 570, (c) 590, and (d) 610 nm track the migration of the bleach across the visible spectrum. At shorter wavelengths an ultrafast bleach recovery was observed, and at longer wavelengths bleach maximum was achieved after pump excitation. This excited-state recovery and growth exhibit the same time constant (0.5 ps), indicating that the processes are connected. (B) Scheme illustrating how the compositional gradient impacts charge carriers. The electronic structure of $CsPbX_3$ dictates that the valence band energy is impacted stronger with the incorporation of iodide, thus leading to preferential hole transfer to iodide-rich film regions at the film surface.

exchange, leading to a single peak with only a minor shift from pure $CsPbBr_3$. Conversely, when pumped from the forward side, excitation spans across a gradient of mixed halide with varying bromide and iodide composition, resulting in the broad bleach seen in Figure 6B.

Under laser pulse excitation from the forward side, the bleach maximum shifts from 565 nm (0.5 ps delay) to 610 nm (10 ps delay) (Figure 6B). This phenomenon was further investigated by analyzing the bleach kinetics of the film side transient spectrum at different wavelengths (Figure 7A). The majority of the bleach at 550 nm (a) recovers in about one picosecond. At longer monitored wavelengths, this initial fast recovery becomes less pronounced and bleach maximum shifts to delay times after pump absorption (spectra b,c). At 610 nm (d), the majority of the bleach occurs after pump absorption with no noticeable ultrafast recovery observed. The temporal shift in bleach maximum at longer wavelengths indicates that a process other than direct pump excitation bleached the sample, as the width of the pump pulse is only 150 fs. Such kinetic profiles are consistent with charge carriers in higher energy

DOI: 10.1021/jacs.6b04661
J. Am. Chem. Soc. 2016, 138, 8603−8611

excited states migrating to lower energy states (Figure 7B). This was confirmed by the ultrafast recovery at 550 nm sharing a time constant of 0.5 ps with the excited-state growth at 620 nm (Figure S18).

We attribute this excited-state behavior in the gradient film to carrier migration into iodide-rich regions near the film surface. The electronic structure of $CsPbX_3$ perovskites indicates that halide and lead dominate in contributions to the valence and conduction bands, respectively.[53,59] Thus, within the compositional gradient, the valence band shifts to higher energies closer to the iodide-rich surface, pulling holes from bromide-rich regions deeper in the film (Figure 7B). The conduction band is not impacted as drastically, and therefore electrons are less influenced by the compositional gradient.

The presence of distinct bromide- and iodide-rich film regions in halide exchanged films is similar to localized iodide- and bromide-rich regions in mixed halide perovskites arising from photoinduced phase separation.[23,57] In photoinduced phase segregated films of $MAPbBr_xI_{3-x}$, hole transfer to iodide-rich film regions results in charge recombination at iodide-rich sites.[57] Such a mechanism could negatively impact the performance of mixed halide perovskites, due to iodide-rich regions acting as hole traps. However, when iodide- and bromide-rich regions are separated in an ordered structure, such as in our halide-exchanged films, holes are preferentially moved toward the film surface. This observed hole-funneling behavior could potentially improve charge separation when implemented into devices by pushing holes toward a hole-conducting medium.

CONCLUSION

In summary, our layer-by-layer deposition procedure for the fabrication of bulk $CsPbBr_3$ from NC sintering does not rely on the solubility of reactant precursors, thus providing an alternative route for the fabrication of $CsPbBr_3$ films. When exposed to a heated PbI_2 solution $CsPbBr_3$ transformed into $CsPbI_3$ via a halide exchange reaction. The exchanged film maintained a cubic crystal phase, providing a simple low-temperature method to obtain bulk cubic $CsPbI_3$. The rate of the exchange reaction was highly dependent upon the temperature of the soaking solution, featuring an Arrhenius relationship. The internal structure of hybrid $CsPbBr_xI_{3-x}$ varied upon the thickness of the exchanged film. This dependence arose from the role of diffusion in the halide exchange reaction. Transient absorption spectroscopy of exchange films revealed that thin films with small amounts of iodide resulted in high rates of recombination. In thicker films, rapid hole transfer to iodide-rich film regions along the built-in compositional was observed. This migration illustrates the potential of such an internal structure in aiding charge separation in $CsPbBr_xI_{3-x}$ mixed halide solar cells.

ASSOCIATED CONTENT

Supporting Information

The Supporting Information is available free of charge on the ACS Publications website at DOI: 10.1021/jacs.6b04661.

TEM images, SEM images, absorption spectra, photoluminescence spectra, Tauc gaps, XRD spectra, reaction kinetics, pump penetration depth, and transient absorption spectra (Figures S1−S18) (PDF)

AUTHOR INFORMATION

Corresponding Author

*pkamat@nd.edu

Present Address

⊥A.L.S.: University of Heidelberg, Germany

Notes

The authors declare no competing financial interest.

ACKNOWLEDGMENTS

The research described herein was supported by the Center for Sustainable Energy at Notre Dame (cSEND) through the Patrick and Jana Eilers Graduate Student Fellowship and by the Division of Chemical Sciences, Geosciences, and Biosciences, Office of Basic Energy Sciences of the U.S. Department of Energy, through award DE-FC02-04ER15533. This is contribution number NDRL No. 5119 from the Notre Dame Radiation Laboratory. The authors would like to thank Dr. Joe Manser for discussions regarding perovskites, Dr. Bill Schneider for discussions involving halide exchange, and Dr. Allen Oliver for discussions on powder XRD.

REFERENCES

(1) Sum, T. C.; Mathews, N. *Energy Environ. Sci.* **2014**, *7*, 2518−2534.
(2) Lewis, N. S. *Science* **2016**, *351*, 353−363.
(3) Hodes, G. *Science* **2013**, *342* (6156), 317−318.
(4) Heo, J. H.; Im, S. H. *Nanoscale* **2016**, *8*, 2554−2560.
(5) Kojima, A.; Teshima, K.; Shirai, Y.; Miyasaka, T. *J. Am. Chem. Soc.* **2009**, *131* (17), 6050−6051.
(6) NREL. Best Research-Cell Efficiencies, http://www.nrel.gov/ncpv/images/efficiency_chart.jpg.
(7) Ponseca, C. S.; Savenije, T. J.; Abdellah, M.; Zheng, K.; Yartsev, A.; Pascher, T.; Harlang, T.; Chabera, P.; Pullerits, T.; Stepanov, A.; Wolf, J. P.; Sundström, V. *J. Am. Chem. Soc.* **2014**, *136* (14), 5189−5192.
(8) Yin, W.-J. W.; Yang, J.-H. J.; Kang, J.; Yan, Y.; Wei, S.-H. *J. Mater. Chem. A* **2015**, *3* (17), 8926−8942.
(9) Yin, W. J.; Shi, T.; Yan, Y. *Adv. Mater.* **2014**, *26* (27), 4653−4658.
(10) Feng, J.; Xiao, B. *J. Phys. Chem. Lett.* **2014**, *5* (7), 1278−1282.
(11) Frost, J. M.; Butler, K. T.; Brivio, F.; Hendon, C. H.; Van Schilfgaarde, M.; Walsh, A. *Nano Lett.* **2014**, *14* (5), 2584−2590.
(12) Oga, H.; Saeki, A.; Ogomi, Y.; Hayase, S.; Seki, S. *J. Am. Chem. Soc.* **2014**, *136* (39), 13818−13825.
(13) Stranks, S. D.; Eperon, G. E.; Grancini, G.; Menelaou, C.; Alcocer, M. J. P.; Leijtens, T.; Herz, L. M.; Petrozza, A.; Snaith, H. J. *Science* **2013**, *342*, 341−344.
(14) Dong, Q.; Fang, Y.; Shao, Y.; Mulligan, P.; Qiu, J.; Cao, L.; Huang, J. *Science* **2015**, *347* (6225), 967−970.
(15) De Wolf, S.; Holovsky, J.; Moon, S. J.; Löper, P.; Niesen, B.; Ledinsky, M.; Haug, F. J.; Yum, J. H.; Ballif, C. *J. Phys. Chem. Lett.* **2014**, *5* (6), 1035−1039.
(16) Xing, G.; Mathews, N.; Sun, S.; Lim, S. S.; Lam, Y. M.; Grätzel, M.; Mhaisalkar, S.; Sum, T. C. *Science* **2013**, *342* (6156), 344−347.
(17) Christians, J. A.; Miranda Herrera, P. A.; Kamat, P. V. *J. Am. Chem. Soc.* **2015**, *137* (4), 1530−1538.
(18) Jiao, Y.; Ma, F.; Gao, G.; Wang, H.; Bell, J.; Frauenheim, T.; Du, A. *RSC Adv.* **2015**, *5* (100), 82346−82350.
(19) Yang, J.; Siempelkamp, B. D.; Liu, D.; Kelly, T. L. *ACS Nano* **2015**, *9* (2), 1955−1963.
(20) Alberti, A.; Deretzis, I.; Pellegrino, G.; Bongiorno, C.; Smecca, E.; Mannino, G.; Giannazzo, F.; Condorelli, G. G.; Sakai, N.; Miyasaka, T.; Spinella, C.; La Magna, A. *ChemPhysChem* **2015**, *16* (14), 3064−3071.
(21) Misra, R. K.; Aharon, S.; Li, B.; Mogilyansky, D.; Visoly-Fisher, I.; Etgar, L.; Katz, E. A. *J. Phys. Chem. Lett.* **2015**, *6* (3), 326−330.

DOI: 10.1021/jacs.6b04661
J. Am. Chem. Soc. 2016, 138, 8603−8611

(22) Han, Y.; Meyer, S.; Dkhissi, Y.; Weber, K.; Pringle, J. M.; Bach, U.; Spiccia, L.; Cheng, Y.-B. *J. Mater. Chem. A* **2015**, *3* (15), 8139−8147.
(23) Beal, R. E.; Slotcavage, D. J.; Leijtens, T.; Bowring, A. R.; Belisle, R. A.; Nguyen, W. H.; Burkhard, G. F.; Hoke, E. T.; Mcgehee, M. D. *J. Phys. Chem. Lett.* **2016**, *7* (5), 746−751.
(24) Wang, Y.; Li, X.; Song, J.; Xiao, L.; Zeng, H.; Sun, H. *Adv. Mater.* **2015**, *27* (44), 7101−7108.
(25) Heidrich, K.; Künzel, H.; Treusch, J. *Solid State Commun.* **1978**, *25* (11), 887−889.
(26) Chang, Y. H.; Park, C. H.; Matsuishi, K. *J. Korean Phys. Soc.* **2004**, *44*, 889−893.
(27) Li, Z.; Yang, M.; Park, J. S.; Wei, S. H.; Berry, J. J.; Zhu, K. *Chem. Mater.* **2016**, *28* (1), 284−292.
(28) Kulbak, M.; Gupta, S.; Kedem, N.; Levine, I.; Bendikov, T.; Hodes, G.; Cahen, D. *J. Phys. Chem. Lett.* **2016**, *7* (1), 167−172.
(29) Kulbak, M.; Cahen, D.; Hodes, G. *J. Phys. Chem. Lett.* **2015**, *6* (13), 2452−2456.
(30) Sharenko, A.; Toney, M. F. *J. Am. Chem. Soc.* **2016**, *138*, 463−470.
(31) Shockley, W.; Queisser, H. J. *J. Appl. Phys.* **1961**, *32* (3), 510−519.
(32) Eperon, G. E.; Stranks, S. D.; Menelaou, C.; Johnston, M. B.; Herz, L. M.; Snaith, H. J. *Energy Environ. Sci.* **2014**, *7*, 982−988.
(33) Yunakova, O. N.; Miloslavskii, V. K.; Kovalenko, E. N. *Opt. Spectrosc.* **2012**, *112* (1), 91−96.
(34) Yunakova, O. N.; Miloslavsky, V. K.; Kovalenko, E. N. *Opt. Spectrosc.* **2014**, *116* (1), 68−71.
(35) Eperon, G. E.; Paterno, G. M.; Sutton, R. J.; Zampetti, A.; Haghighirad, A. A.; Cacialli, F.; Snaith, H. J. *J. Mater. Chem. A* **2015**, *3* (39), 19688−19695.
(36) Stoumpos, C. C.; Malliakas, C. D.; Kanatzidis, M. G. *Inorg. Chem.* **2013**, *52* (15), 9019−9038.
(37) Li, G.; Ho, J. Y.-L.; Wong, M.; Kwok, H. S. *J. Phys. Chem. C* **2015**, *119* (48), 26883−26888.
(38) Pellet, N.; Teuscher, J.; Maier, J.; Grätzel, M. *Chem. Mater.* **2015**, *27* (6), 2181−2188.
(39) Solis-Ibarra, D.; Smith, I. C.; Karunadasa, H. I. *Chem. Sci.* **2015**, *6* (7), 4054−4059.
(40) Nedelcu, G.; Protesescu, L.; Yakunin, S.; Bodnarchuk, M. I.; Grotevent, M. J.; Kovalenko, M. V. *Nano Lett.* **2015**, *15* (8), 5635−5640.
(41) Akkerman, Q. A.; D'Innocenzo, V.; Accornero, S.; Scarpellini, A.; Petrozza, A.; Prato, M.; Manna, L. *J. Am. Chem. Soc.* **2015**, *137* (32), 10276−10281.
(42) Protesescu, L.; Yakunin, S.; Bodnarchuk, M. I.; Krieg, F.; Caputo, R.; Hendon, C. H.; Yang, R. X.; Walsh, A.; Kovalenko, M. V. *Nano Lett.* **2015**, *15* (6), 3692−3696.
(43) Lakowicz, J. R. *Principles of Fluorescence Spectroscopy*; Springer US: Boston, MA, 2006.
(44) Macdonald, B. I.; Martucci, A.; Rubanov, S.; Watkins, S. E.; Mulvaney, P.; Jasieniak, J. J. *ACS Nano* **2012**, *6* (7), 5995−6004.
(45) Yakunin, S.; Protesescu, L.; Krieg, F.; Bodnarchuk, M. I.; Nedelcu, G.; Humer, M.; De Luca, G.; Fiebig, M.; Heiss, W.; Kovalenko, M. V. *Nat. Commun.* **2015**, *6*, 8056.
(46) Pan, J.; Sarmah, S. P.; Murali, B.; Dursun, I.; Peng, W.; Parida, M. R.; Liu, J.; Sinatra, L.; Alyami, N.; Zhao, C.; Alarousu, E.; Ng, T. K. K.; Ooi, B. S.; Bakr, O. M.; Mohammed, O. F. *J. Phys. Chem. Lett.* **2015**, *6* (24), 5027−5033.
(47) Gao, Y.; Zhu, J.; Tian, Y.; Qin, D. *Phys. E* **2014**, *60*, 17−22.
(48) Truong, N. T. N.; Trinh, K. T.; Pham, V. T. H.; Kim, C. D.; Park, C. *Korean J. Chem. Eng.* **2015**, *32* (4), 761−766.
(49) De Roo, J.; Ibáñez, M.; Geiregat, P.; Nedelcu, G.; Walravens, W.; Maes, J.; Martins, J. C.; Van Driessche, I.; Kovalenko, M. V.; Hens, Z. *ACS Nano* **2016**, *10* (2), 2071−2081.
(50) Bekenstein, Y.; Koscher, B. a.; Eaton, S. W.; Yang, P.; Alivisatos, a. P. *J. Am. Chem. Soc.* **2015**, *137* (51), 16008−16011.
(51) Srimath Kandada, A. R.; Petrozza, A. *Acc. Chem. Res.* **2016**, *49* (3), 536−544.
(52) D'Innocenzo, V.; Grancini, G.; Alcocer, M. J. P.; Kandada, A. R. S.; Stranks, S. D.; Lee, M. M.; Lanzani, G.; Snaith, H. J.; Petrozza, A. *Nat. Commun.* **2014**, *5*, 3586.
(53) Murtaza, G.; Ahmad, I. *Phys. B* **2011**, *406* (17), 3222−3229.
(54) Eperon, G. E.; Stranks, S. D.; Menelaou, C.; Johnston, M. B.; Herz, L. M.; Snaith, H. J. *Energy Environ. Sci.* **2014**, *7* (3), 982.
(55) Fedorov, V. A.; Ganshin, V. A.; Korkishko, Y. N. *Phys. Status Solidi A* **1993**, *139* (1), 9−65.
(56) Beberwyck, B. J.; Surendranath, Y.; Alivisatos, A. P. *J. Phys. Chem. C* **2013**, *117* (39), 19759−19770.
(57) Hoke, E. T.; Slotcavage, D. J.; Dohner, E. R.; Bowring, A. R.; Karunadasa, H. I.; McGehee, M. D. *Chem. Sci.* **2015**, *6* (1), 613−617.
(58) Stamplecoskie, K. G.; Manser, J. S.; Kamat, P. V. *Energy Environ. Sci.* **2015**, *8* (1), 208−215.
(59) Huang, L. Y.; Lambrecht, W. R. L. *Phys. Rev. B: Condens. Matter Mater. Phys.* **2013**, *88*, 165203.

DOI: 10.1021/jacs.6b04661
J. Am. Chem. Soc. 2016, 138, 8603−8611